Reversible structure manipulation by tuning carrier concentration in metastable Cu_2S

Jing Tao[a,1], Jingyi Chen[b,1], Jun Li[a], Leanne Mathurin[b], Jin-Cheng Zheng[c,d], Yan Li[e], Deyu Lu[f], Yue Cao[a], Lijun Wu[a], Robert Joseph Cava[g,1], and Yimei Zhu[a]

[a]Condensed Matter Physics & Materials Science Department, Brookhaven National Laboratory, Upton, NY 11973; [b]Department of Chemistry and Biochemistry, University of Arkansas, Fayetteville, AR 72701; [c]Department of Physics, and Collaborative Innovation Center for Optoelectronic Semiconductors and Efficient Devices, Xiamen University, Xiamen 361005, China; [d]High Performance Computing Center, Xiamen University Malaysia, 439000 Sepang, Selangor, Malaysia; [e]American Physical Society, Ridge, NY 11961; [f]Center for Functional Nanomaterials, Brookhaven National Laboratory, Upton, NY 11973; and [g]Department of Chemistry, Princeton University, Princeton, NJ 08544

Contributed by Robert Joseph Cava, July 27, 2017 (sent for review June 5, 2017; reviewed by Albina Y. Borisevich and Ray Egerton)

The optimal functionalities of materials often appear at phase transitions involving simultaneous changes in the electronic structure and the symmetry of the underlying lattice. It is experimentally challenging to disentangle which of the two effects—electronic or structural—is the driving force for the phase transition and to use the mechanism to control material properties. Here we report the concurrent pumping and probing of Cu_2S nanoplates using an electron beam to directly manipulate the transition between two phases with distinctly different crystal symmetries and charge-carrier concentrations, and show that the transition is the result of charge generation for one phase and charge depletion for the other. We demonstrate that this manipulation is fully reversible and nonthermal in nature. Our observations reveal a phase-transition pathway in materials, where electron-induced changes in the electronic structure can lead to a macroscopic reconstruction of the crystal structure.

Cu_2S | phase transition | structure manipulation | electron-beam–radiation effects

Recent years have witnessed a blurring of the edges between functional and quantum materials—the key properties of functional materials are often born out of strong structural and electronic interactions that are quantum mechanical in nature. Notable examples include colossal magnetoresistance manganites (1), ferroelectrics (2), and valleytronic materials (3). The targeted functions are usually accompanied by symmetry breaking, induced through changes in temperature or under other external perturbations. A prominent question is whether the symmetry reduction has an origin in the lattice (e.g., in the form of displacement of atoms, and could be described reasonably well using first-principles calculations) or the electronic degrees of freedom (charge, spin, and orbital) (4–6). It is of great interest to distinguish the roles of these factors in phase transitions.

Cu_2S provides an intriguing example for addressing the above "chicken-and-egg" question (6), which is critical to the understanding of a wide range of functional and quantum materials. It is a fast ionic conductor (7) with highly mobile Cu ions. A phase transition in the bulk material occurs near 100 °C from a semiconducting (8) monoclinic symmetry low-chalcocite phase (9) [hereafter called the "L-s phase" (i.e., low, semiconducting); space group $P2_1/c$] to an electrically insulating (10) hexagonal symmetry high-chalcocite phase (7, 11) [hereafter called the "H-i phase" (i.e., high, insulating); space group $P6_3/mmc$]. The coinciding changes in the bulk electrical conductivity and crystal structure present a possibility for exploring the relationship between electronic and structural phase transitions. Difficulties in the synthesis of stoichiometric Cu_2S material and the lack of detailed theoretical treatments of both the crystal and the electronic structures of Cu_2S have hindered the understanding of the phase transition (7, 11–13).

Results and Discussion

We have recently synthesized high-quality Cu_2S nanoplates (*Materials and Methods*), which are on the order of 10-nm thick and 100 nm in lateral dimension (Fig. 1 *A* and *B*). Electron diffraction patterns (Fig. 1*C*) obtained in a transmission electron microscope (TEM) from individual plates along the [001] zone axis indicate that the nanoplates exhibit a single-crystalline structural transition from the L-s phase (left half) to the H-i phase (right half) upon heating. The transition temperature of the nanoplates (~80 °C), which occurs abruptly on heating and cooling, is somewhat lower than that of bulk Cu_2S (~100 °C). The small suppression of the phase-transition temperature observed here for Cu_2S nanoplates is consistent with previous studies on nanomaterials (14). The corresponding crystal structures of the L-s and H-i phases are displayed schematically in Fig. 1 *D* and *E*, respectively. At room temperature, the strongest reflections in the electron diffraction pattern obtained from the L-s phase have nearly hexagonal symmetry, but the observable superlattice reflections resulting from the structural modulation that makes the L-s phase monoclinic are also present. The electron diffraction pattern obtained from the H-i phase is purely hexagonal, with no superlattice—reflecting the absence of a structural modulation in this phase. Previous resistivity studies at various levels of nonstoichiometry in $Cu_{2-x}S$ showed that the phase transition is abrupt on heating and cooling only when the Cu vacancies (x) present are less than 1% of the atomic weight (15), thus confirming the stoichiometry of our nanoparticles. Since Cu vacancies are acceptors in Cu_2S, the hole carrier (hereafter denominated as "e^+") concentration in our p-type nanoplates $n_e{}^+$ is less than 1%. The

Significance

Harnessing a material's functionality in applications and for fundamental studies often requires direct manipulation of its crystal symmetry. We manipulate the crystal structure of Cu_2S nanoparticles in a controlled and reversible fashion via variation of the electron dose rate, observed by transmission electron microscopy. Our control method is in contrast to conventional chemical doping, which is irreversible and often introduces unwanted lattice distortions. Our study sheds light on the much-debated question of whether a change in electronic structure can facilitate a change of crystal symmetry, or whether vice versa is always the case. We show that a minimal perturbation to the electronic degree of freedom can drive the structural phase transition in Cu_2S, hence resolving this dilemma.

Author contributions: J.T. and J.C. designed research; J.T., J.C., J.L., L.M., J.-C.Z., Y.L., D.L., L.W., R.J.C., and Y.Z. performed research; J.T., J.C., J.-C.Z., and R.J.C. analyzed data; and J.T., J.C., J.L., Y.L., D.L., Y.C., R.J.C., and Y.Z. wrote the paper.

Reviewers: A.Y.B., Oak Ridge National Laboratory; and R.E., University of Alberta.

The authors declare no conflict of interest.

Freely available online through the PNAS open access option.

[1]To whom correspondence may be addressed. Email: jtao@bnl.gov, chenj@uark.edu, or rcava@princeton.edu.

This article contains supporting information online at www.pnas.org/lookup/suppl/doi:10.1073/pnas.1709163114/-/DCSupplemental.

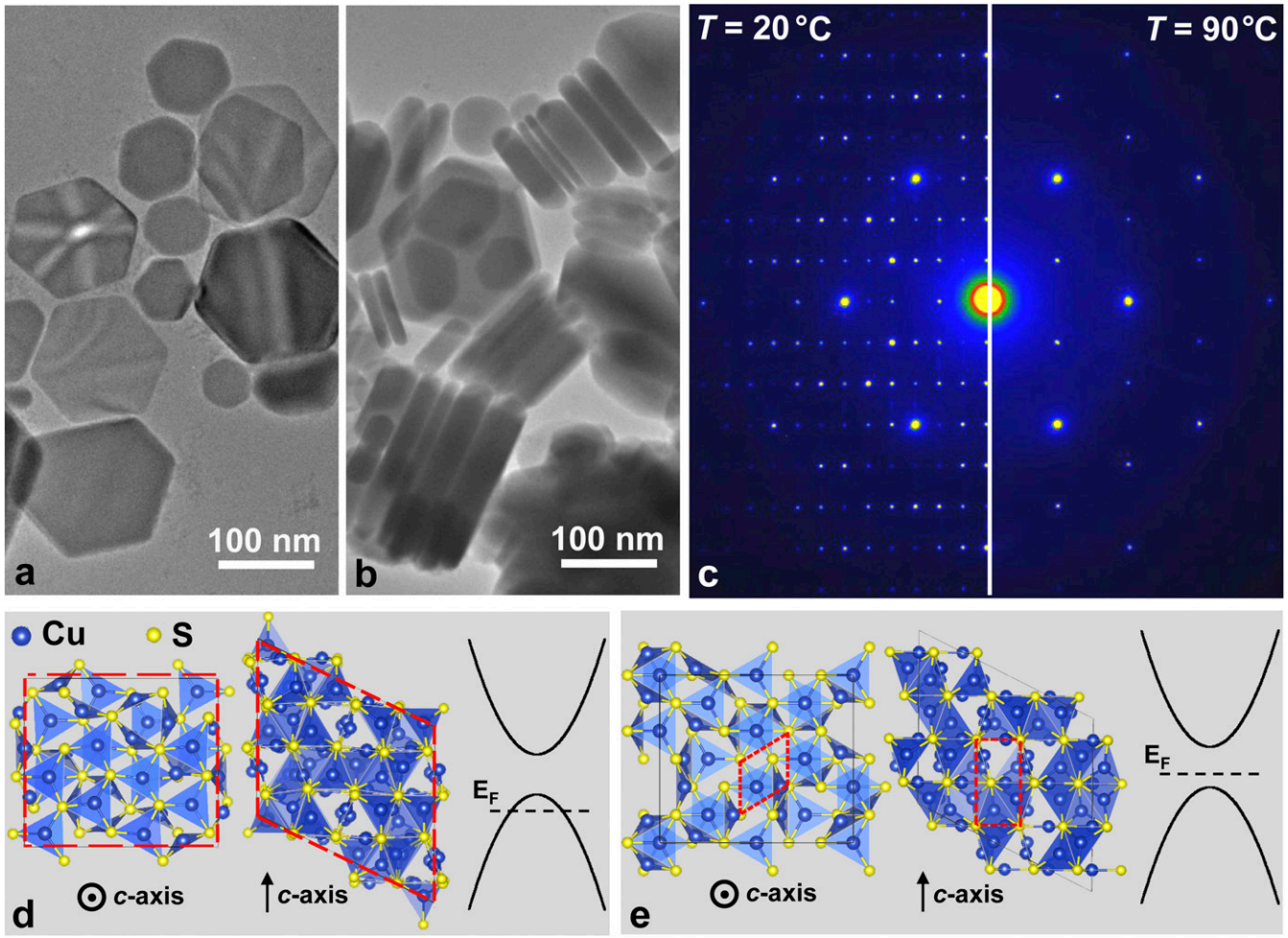

Fig. 1. Structure and morphology of the Cu_2S nanoplates. (*A* and *B*) Typical morphology of Cu_2S nanoplates viewed in-plane (*A*) and edge-on (*B*). The lateral size and thickness of the nanoplates range from 50–200 nm and 10–40 nm (estimated from the "edge-on" plates stacked horizontally on the TEM grid), respectively. (*C*) Electron diffraction patterns obtained from an individual Cu_2S nanoplate at two different temperatures, showing diffraction from the low-chalcocite (L-s phase) structure at 20 °C on the left and from the high-chalcocite (H-i phase) structure at 90 °C on the right. The crystal structures are illustrated in *D* for the L-s phase and *E* for the H-i phase, in two perpendicularly orientated views. The H-i phase structure (*E*) is portrayed using a supercell equivalent to the L-s phase's monoclinic unit cell to facilitate the comparison. [The Cu ions in the H-i phase are placed randomly in the symmetry-allowed positions (7) that have partial occupancies, following the procedure in ref. 12.] For simplicity, only two sulfur planes are shown in the rectangular views. The unit cell of the structure is indicated by red dashed lines. Schematics of the electronic band structures for the two phases are presented in *D* and *E*. Carriers are holes (e^+) in the L-s phase Cu_2S (*D*), while the H-i phase Cu_2S has few e^+ but mobile Cu ions and is considered as an electrical insulator (*E*).

measured [using transport (16)] and calculated electronic structures (8) both report a bandgap of ∼1.5 eV for the H-i phase, while similar analysis of the L-s phase supports semiconducting behavior (8, 17).

During characterization of the Cu_2S nanoplates at room temperature, unexpected phase transitions were observed: We found that the electron diffraction pattern from an individual nanoplate oscillates abruptly between the L-s and H-i phases as the electron dose rate is monotonically increased. These observations were recorded in both reciprocal space and real space for more than 20 nanoplates and are highly reproducible (Movies S1 and S2). A typical series of electron diffraction patterns is shown in Fig. 2*A*, showing the alternating crystal structures as a function of electron dose rate. As the dose rate is increased smoothly (i.e., monotonically), a nanoplate undergoes a series of L-H–L-H transitions. Importantly for elucidating a mechanism for the transitions, the reverse sequence is observed when electron dose rate is smoothly decreased. Typical TEM images together with their corresponding fast Fourier transform (FFT) diffraction patterns, taken at different electron dose rates, provide a good real-space visualization of the structural transitions from the same nanoplate for which the electron diffractions were obtained (Fig. 2*B*). The H-i phase structure exhibits threefold rotational symmetry. Thus, the L-s phase structural modulation can appear in any one of three equivalent orientations in the H-i phase upon each H-L transition during the oscillation process.

We emphasize that, relevant to their origin, the oscillating transitions observed as a function of electron dose rate were found to be reversible and reproducible in a controlled manner. In particular, the structural transition and its products are very robust and do not vary with time under a fixed dose rate during continuous electron illumination. Aside from some hysteresis in the vicinity of the transitions through the cycles of dose-rate increase and decrease, the structural phase observed was found to be explicitly determined by the electron dose rate (Table S1).

Because changes in temperature can lead to structural phase transitions, the effect of temperature on the phase transitions in our Cu_2S nanoplates was further explored using in situ TEM. The experiments resulted in the construction of a temperature–dose-rate phase diagram for individual Cu_2S nanoplates (Fig. 3).

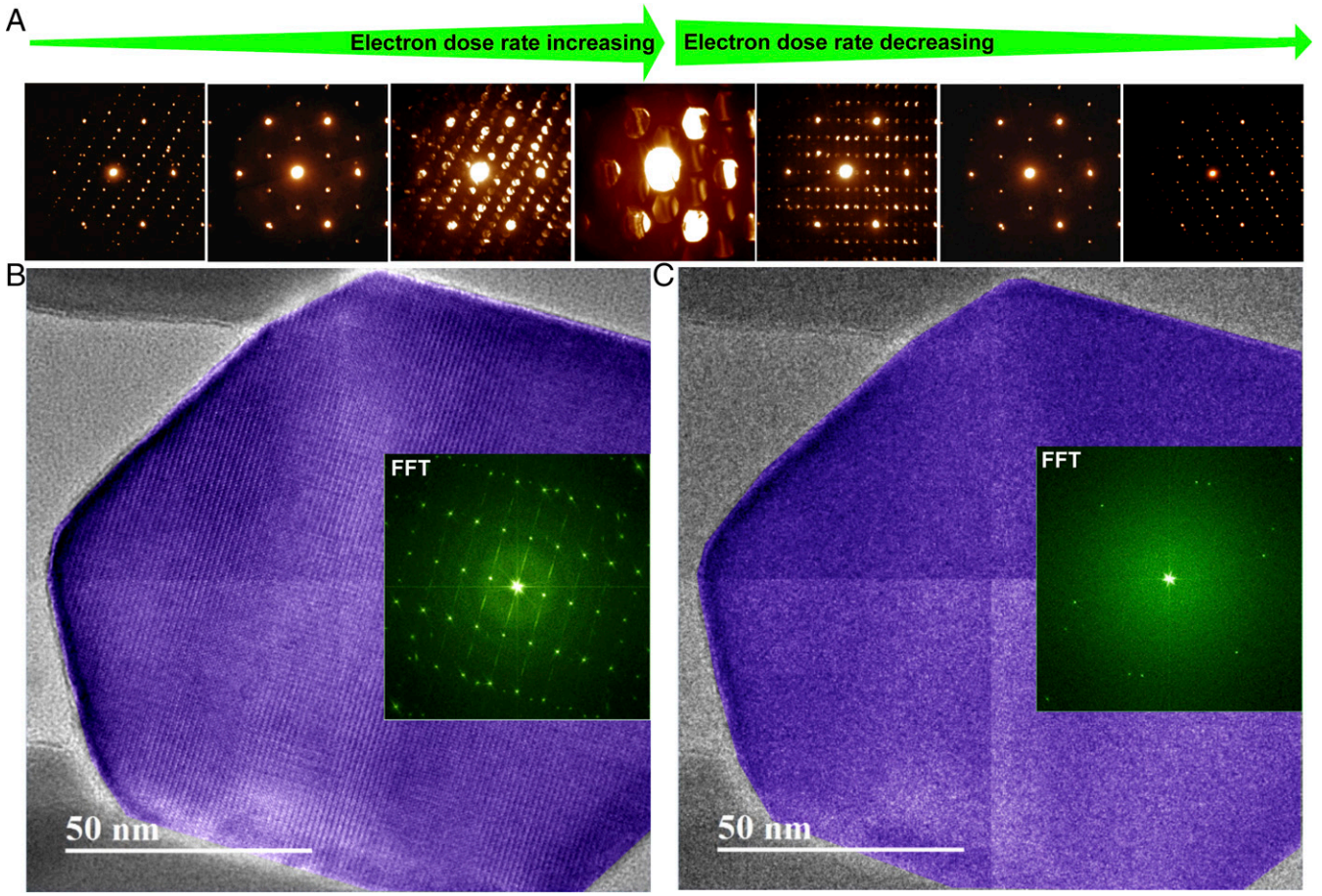

Fig. 2. Structural evolution of a Cu_2S nanoplate under an electron dose-rate cycle at room temperature. (*A*) Snapshots of the electron diffraction patterns on increasing and decreasing the electron dose rate. (*B* and *C*) Typical real-space lattice images with their FFTs. In the diffraction series, an L-H–L-H structural transition can be identified when the electron dose rate is monotonically increased, and a reversible H-L–H-L structural transition is recorded as the electron dose rate is monotonically decreased. Because the electron dose rate increases by focusing the electron beam, higher electron dose rate corresponds to larger convergent beam angle and consequently larger reflection spots in the electron diffraction patterns. The lattice images were selected from an imaging series under the electron dose cycle and show the same Cu_2S nanoplate in the L-s phase in *B* and the H-i phase in *C*.

The resulting phase diagram is unexpected and yet highly reproducible. An individual nanoplate remains in the L-s phase at temperatures below 5 °C for all electron dose rates. The oscillating phase transition, L-H–L-H, as a function of electron dose rate, occurs only in a narrow temperature regime between ∼5 °C and ∼40 °C. Above ∼40 °C but below ∼80 °C, only a single L-H phase transition is observed (i.e., there is no oscillation) at the low incident–electron current of a few picoamperes (a picoampere, "pA," is 10^{-12} Coulombs of charge per second or 6.24×10^6 electrons per second; the electron dose-rate readings in the microscope at the sample position are in the units of $A{\cdot}nm^{-2}$, i.e., $Coulomb{\cdot}s^{-1}{\cdot}nm^{-2}$. The plotted and listed incident–electron currents due to the electron illumination in the entire article were obtained from the microscope dose-rate reading in Coulomb s^{-1} nm^{-2} through multiplying by the area of the nanoplate) on an individual nanoplate ($\sim 9.4 \times 10^3$ nm^2; such plate is about 120 nm in size from corner to corner along the diagonal direction. Therefore, the incident–electron current is linearly proportional to the electron dose rate on the nanoplate). Finally, no phase transition is observed at any incident–electron current for nanoplates at temperatures above 80 °C; the nanoplates stay in the H-i phase. The scenario at room temperature, fortuitously in the temperature regime where the oscillatory phase transitions are observed (dashed line in Fig. 3), demonstrated in Fig. 2, is further illustrated in Fig. 4*B*, showing the presence of hysteresis in the electron dose-rate dependence of the phase transitions during the process.

It is of interest to unravel the role of the electron dose rate in inducing the structural transitions in the Cu_2S nanoplates. In general, electron-beam illumination is known to cause ionization, heating, electrostatic charging, and knock-on damage in materials (18–21). These possible effects were therefore investigated. Our electron-energy-loss spectra (EELS) acquired from individual nanoplates showed no detectable difference in the fine structure of the Cu-L edge between the L-s and H-i phases (Fig. S1); this rules out the possibility of a significant amount of Cu ionization during electron irradiation. A heating effect, which would be directly proportional to the electron dose rate, can be excluded as the dominant driving force for several reasons. Firstly, if the nanoplate temperature is made to rise due to the electron-beam heating, then the crystal phase of the nanoplate would not oscillate back and forth with increasing electron dose rate: A single L-s to H-i transition might be observed on increasing the dose rate (increased dose rate would supply more energy for heating in this scenario), but L-H–L-H oscillations would not be possible. Secondly, if an incident–electron current of ∼20 pA (i.e., 1.25×10^7 electrons per second), which accounts for the first L-H transition of an individual nanoplate at 20 °C, could hypothetically heat up the nanoplate and cause an L-H transition due to heating above the transition temperature at

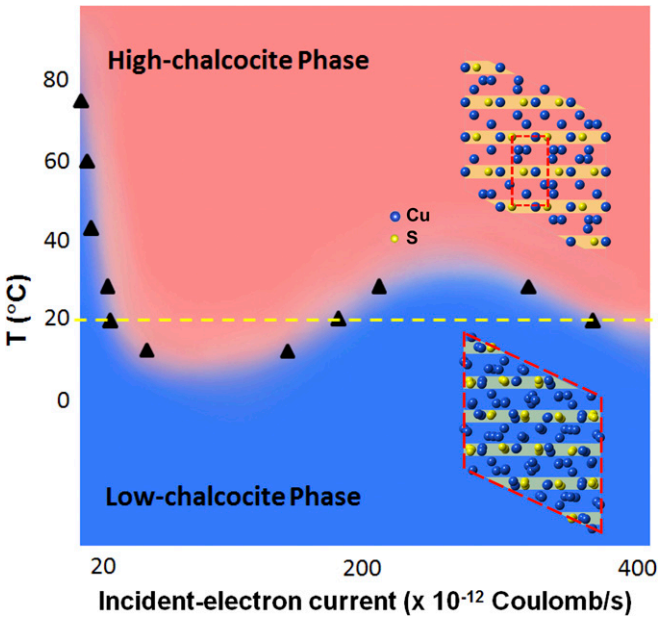

Fig. 3. Structural phase diagram of Cu_2S nanoplates. The structural phase diagram (temperature of the L-H phase transition as a function of electron dose rate) constructed from TEM experiments from individual Cu_2S nanoplates. Incident–electron current values from individual nanoplate at the transitions are shown as black triangles (see Table S2 for specific current values). The structures of different phases are also shown, with their unit cells highlighted. Following the yellow dashed line indicates the sequence of transitions as a function of dose rate at room temperature and is summarized in Fig. 2. Note that the electron dose-rate readings in the microscope at the sample position are in the units of Coulomb·s^{-1}·nm^{-2}, i.e., 6.24×10^{18} electrons·s^{-1}·nm^{-2}. The plotted incident–electron currents were obtained from the microscope dose-rate reading in Coulomb·s^{-1}·nm^{-2} through multiplying by the area of the nanoplate (~9.4×10^3 nm^2) where the observation was obtained.

80 °C, it is impossible that a 400-pA electron current (20× the power input) would be unable to raise the temperature of the nanoplate from 5 to 80 °C (a ΔT difference of only 15 °C); at 5 °C the nanoplates are observed to remain in their L-s phase regardless of the electron dose rate. Moreover, the fact that the oscillation of the transition is reversible, occurring both on increasing the electron dose rate from its minimum and decreasing the dose rate from its maximum, indicates that no irreversible changes in the material stoichiometry or crystalline perfection could have occurred during the electron dose process; irreversible processes such as mass loss or hydrocarbon contamination also could not have occurred. Finally, the knock-on mechanism, which describes the direct displacement of atoms from the crystal lattice by the incident–electron beam, and is a function of the energy of the incident beam voltage, can also be considered as a possible effect taking place during the observations. With the energy transfer from the incident beam to the Cu_2S material, Cu and S could move from their original positions. However, the L-H transition should follow thermodynamic rules, and thus although we did not explicitly exclude the possibility, it is unlikely that the knock-on mechanism plays a central role in our observations because it is hard to imagine how it could result in the observed oscillating phase transition as a function of monotonically changing beam dose rate. Nevertheless, the knock-on effect can be very complicated in this material and it would be interesting to further examine the mechanism using an electron beam with various incident energies in the future.

Based on all of the considerations above, we propose that electrostatic charging is the driving mechanism for the phase transition. The process is schematically illustrated in Fig. 4. Electron illumination generates secondary and Auger electrons inside the thin samples during the TEM observations. When this is combined with poor electrical conductivity, positive charges can build up due to the escape of the secondary and Auger electrons from the sample (18, 19, 22–25). For Cu_2S, the difference in the band gaps of the semiconducting L-s phase and the insulating H-i phase, meaning that their Fermi levels are at different energies, gives rise to drastic changes in the charge distribution throughout the nanoplate volumes during the electron-beam–radiation process. In the case of metals and semiconductors, secondary and Auger electrons can only escape from the top surface of a material—the typical escape depth is smaller than 1 nm for secondary electrons in metals (19). Thus, in the semiconducting L-s phase of the nanoplates, positive charge accumulates only at the top surface, resulting in the presence of an electrostatic field (19, 23). This causes a depletion of the existing positive carriers, i.e., the e^+.

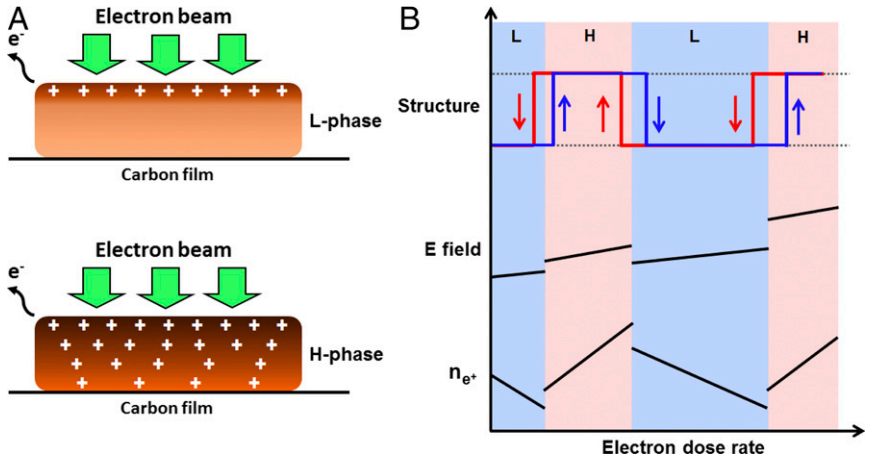

Fig. 4. Role of electron dose rate in the structural transitions. (*A*) Schematic of positive charge distribution induced by the electron illumination in the nanoplates during the phase transitions. Secondary and Auger electrons are generated from the electron-beam illumination and can escape from the nanoplate, leaving the nanoplate positively charged and creating a static electric field inside the nanoplate. In the L-s phase, only the top surface is positively charged, causing a charge depletion of the existing e^+ carriers (*A, Top*), while the e^+ concentration is increased to a high level induced by the electron illumination (*A, Bottom*). (*B*) Structural phase transition as a function of the electron dose rate at room temperature (indicated by the yellow dashed line in Fig. 3), buildup electric field inside a nanoplate, and e^+ concentration (n_{e^+}) are plotted as a function of electron dose rate during the phase transitions.

On the other hand, in an electronic insulator, the escape depth for secondary and Auger electrons is widely accepted to be on the order of tens of nanometers (19, 24, 25), at least an order of magnitude larger than in a semiconducting phase. Assuming an exponential decay of the charge distribution along the incident–electron-beam direction (Fig. S2), this long escape depth when combined with the thin nanoplates directly leads to a significant e^+ density in the full volume in the insulating H-i phase, with a static electric field that is also perpendicular to the top surface of the nanoplate.

The result is a redistribution of the electronic charge during electron radiation. The observed structures, average electric field, and e^+ concentration are plotted in Fig. 4*B* as a function of electron dose rate. Note that we can only observe the "quasi-steady" state where charge generation and redistribution has reached a dynamical balance for a given electron dose rate (Fig. S3). This dynamical balance takes place on a timescale faster than can be observed in conventional electron diffraction, and thus the kinetics of the transformation is outside the scope of the current discussion.

Combining the TEM observations and analysis of the electron pumping mechanisms, it can be concluded that the structural phase transitions observed in Cu_2S nanoplates under TEM illumination are driven by the change of positive carrier e^+ concentration and redistribution in the nanoplates. The electron beam probes the structures of the nanoplates while inducing two competing processes. One process is to deplete the existing e^+ from the nanoplate volume as charge accumulates at the top surface. The other is to generate e^+ as a natural result of electron illumination, maintaining the concentration of positive carriers at a finite level in the volume of the nanoplate. The charge-depletion mechanism dominates in the L-s phase while the charge-generating mechanism dominates in the H-i phase. In the L-s phase, the e^+ concentration is mainly determined by the strength of the static electric field induced by the electron beam (Fig. 4*B*). Namely, the higher the electron dose rate applied, the lower the e^+ concentration in the L-s nanoplate. On the other hand, where the charge-generation mechanism dominates (in the H-i phase), the influence of the electric field on the e^+ concentration is significantly weakened; instead, the e^+ concentration is directly proportional to the electron dose rate. As a result, with increasing electron dose rate, the e^+ concentration in each, together with the Fermi level, changes in a direction that makes the other phase more energetically favorable (Fig. 4*B*). This leads to the oscillating phase transitions observed in this work. The critical electron dose rates for the transitions mark where the total energies of the L-s and H-i phases are essentially the same. Further increase or decrease of the electron dose rates tips the energy balance, giving rise to the phase transition.

This electronically driven structural phase-transition mechanism can explain very well the origin of puzzling previously reported results obtained from Cu_2S, including its anomalous switching behavior under voltage pulses (13). The electron pumping mechanism across a structural phase transition that we observe for Cu_2S nanoplates will no doubt also be operating in other metastable and nonequilibrium phases as well, and for metal–insulator phase transitions in general in nanoparticles of complex materials (26–28).

The subtle electronic and lattice structure differences between the L-s and H-i phases in Cu_2S are of importance in revealing the influence of the underlying physics, such as electron–phonon coupling, in the observed carrier-concentration-induced structural transition. The discussion for the crystal structure of the H-i phase can be found in Fig. S4. Because the oscillatory character of the phase transition in a Cu_2S nanoplate highly depends on the temperature, as demonstrated in the phase diagram in Fig. 3*A*, phonons are likely to play a significant role in the transition mechanism. In particular, anharmonic lattice dynamics has been proposed to be critical in the understanding of the thermal/transport properties in Cu_2S (7) and the electric-field-driven transition in VO_2 (29). In light of the strong interplay between degrees of freedom that often gives rise to gigantic effects and "electronically soft" behavior in correlated materials (30), unusual coupling between charge and phonons is anticipated to be responsible for the "structurally soft" behavior in Cu_2S.

Materials and Methods

Synthesis of Cu_2S Nanoplates. The Cu_2S nanoplates were obtained by thermal decomposition of Cu precursors that contain trace amount of sulfur at a concentration of ∼0.2 ppm by weight. In a typical synthesis, copper(II) 2,4-pentanedionate (52.5 mg; Alfa Aesar, 98%), copper(II) chloride anhydrous $CuCl_2$ (41.1 mg; Alfa Aesar, 98%), and 1-dodecylamine (5 g; Alfa Aesar, 98%+) were added to a 25-mL three-neck round-bottom flask equipped with a magnetic stir bar. The solid mixture was degassed with argon for 15 min to remove oxygen, and then heated to 220 °C. The reaction was allowed to proceed for 48 h before the reaction was quenched by removing the reaction from the heating mantel. As the reaction temperature was cooled to 180 °C, the solution was removed from the reaction flask and placed into a 15-mL centrifuge tube containing ethanol. The product was collected by centrifuging at 6,000 rpm/4,185 × *g* (VWR Clinical 200 centrifuge) for 4 min and further purified by ethanol/toluene (1:10 vol/vol) mixture twice before it was redispersed in toluene for future use.

TEM Analysis. TEM experiments were carried out using a JEOL ARM200 microscope (accelerating voltage = 200 kV) with double Cs correctors as well as a JEOL 2100F microscope (accelerating voltage = 200 kV), both equipped with Gatan heating and cooling holders.

ACKNOWLEDGMENTS. We thank Dr. P. D. Johnson and Dr. W. G. Yin for their discussion of the work. We also thank Erik Pollack for help with the ICP-MS measurement at the Arkansas Mass Spectrometry facility. Research was sponsored by the US Department of Energy (DOE) Basic Energy Sciences (BES), by the Materials Sciences and Engineering Division under Contract DE-SC0012704. J.L. was fully supported by the DOE BES Early Career Award Program at Brookhaven National Laboratory under Contract DE-SC0012704. D.L. was supported by the resources of the Center for Functional Nanomaterials, which is a US DOE Office of Science Facility, at Brookhaven National Laboratory. J.-C.Z. was supported by the National Natural Science Foundation of China (11335006 and 51661135011). J.C. and L.M. were supported in part by the University of Arkansas and the National Science Foundation (NSF) through the Center for Advanced Surface Engineering under Grant OIA-1457888 and the Arkansas EPSCoR Program, ASSET III (to J.C.). The work at Princeton University was supported by the NSF Materials Research Science and Engineering Centers Program, Grant DMR-1420541.

1. Salamon MB, Jaime M (2001) The physics of manganites: Structure and transport. *Rev Mod Phys* 73:583–628.
2. Cheong SW, Mostovoy M (2007) Multiferroics: A magnetic twist for ferroelectricity. *Nat Mater* 6:13–20.
3. Schaibley JR, et al. (2016) Valleytronics in 2D materials. *Nat Rev Mater* 1:16055.
4. Nakano M, et al. (2012) Collective bulk carrier delocalization driven by electrostatic surface charge accumulation. *Nature* 487:459–462.
5. McLeod AS, et al. (2016) Nanotextured phase coexistence in the correlated insulator V_2O_3. *Nat Phys* 13:80–87.
6. Fernandes RM, Chubukov AV, Schmalian J (2014) What drives nematic order in iron-based superconductors? *Nat Phys* 10:97–104.
7. Cava RJ, Reidinger F, Wuensch BJ (1981) Mobile ion distribution and anharmonic thermal motion in fast ion conducting Cu_2S. *Solid State Ion* 5:501–504.
8. Xu Q, et al. (2012) Crystal and electronic structures of Cu_xS solar cell absorbers. *Appl Phys Lett* 100:061906.
9. Evans HT (1971) Crystal structure of low chalcocite. *Nature* 232:69–70.
10. Okamoto K, Kawai S (1973) Electrical conduction and phase transition of copper sulfides. *Jpn J Appl Phys* 12:1130–1138.
11. Buerger MJ, Wuensch BJ (1963) Distribution of atoms in high chalcocite, Cu_2S. *Science* 141:276–277.
12. Wang LW (2012) High chalcocite Cu_2S: A solid-liquid hybrid phase. *Phys Rev Lett* 108: 085703.
13. Sakamoto T, et al. (2003) Nanometer-scale switches using copper sulfide. *Appl Phys Lett* 82:3032–3034.
14. Rivest JB, Fong L-K, Jain PK, Toney MF, Alivisatos AP (2011) Size dependence of a temperature-induced solid-solid phase transition in copper(I) sulfide. *J Phys Chem Lett* 2:2402–2406.
15. He Y, et al. (2014) High thermoelectric performance in non-toxic earth-abundant copper sulfide. *Adv Mater* 26:3974–3978.
16. Liu G, Schulmeyer T, Brotz J, Klein A, Jaegermann W (2003) Interface properties and band alignment of Cu2S/CdS thin film solar cells. *Thin Solid Films* 431–432: 477–482.

17. Zhang Y, et al. (2014) Electronic structure of antifluorite Cu_2X (X = S, Se, Te) within the modified Becke-Johnson potential plus an on-site Coulomb U. *J Chem Phys* 140:074702.
18. Egerton RF, Li P, Malac M (2004) Radiation damage in the TEM and SEM. *Micron* 35: 399–409.
19. Cazaux J (1995) Correlations between ionization radiation damage and charging effects in transmission electron microscopy. *Ultramicroscopy* 60:411–425.
20. Zheng H, et al. (2011) Observation of transient structural-transformation dynamics in a Cu_2S nanorod. *Science* 333:206–209.
21. Jesse S, et al. (2015) Atomic-level sculpting of crystalline oxides: Toward bulk nanofabrication with single atomic plane precision. *Small* 11:5895–5900.
22. Larson DM, Downing KH, Glaeser RM (2011) The surface of evaporated carbon films is an insulating, high-bandgap material. *J Struct Biol* 174:420–423.
23. Glaeser RM, Downing KH (2004) Specimen charging on thin films with one conducting layer: Discussion of physical principles. *Microsc Microanal* 10:790–796.
24. Shih A, Yater J, Hor C, Abrams R (1997) Secondary electron emission studies. *Appl Surf Sci* 111:251–258.
25. Kanaya K, Ono S, Ishigaki F (1978) Secondary electron emission from insulators. *J Phys D Appl Phys* 11:2425–2437.
26. Qi Y, Liu S, Lindenberg AM, Rappe AM (2017) Ultra-fast electric field control of giant electrocaloric effect in ferroelectrics. arXiv:1701.02019.
27. Ichikawa H, et al. (2011) Transient photoinduced 'hidden' phase in a manganite. *Nat Mater* 10:101–105.
28. Han T-RT, et al. (2015) Exploration of metastability and hidden phases in correlated electron crystals visualized by femtosecond optical doping and electron crystallography. *Sci Adv* 1:e1400173.
29. Budai JD, et al. (2014) Metallization of vanadium dioxide driven by large phonon entropy. *Nature* 515:535–539.
30. Milward GC, Calderón MJ, Littlewood PB (2005) Electronically soft phases in manganites. *Nature* 433:607–610.
31. Bieniulis MZ, Corry CE, Hoskins ER (1987) Ferroelectricity in natural samples of chalcocite, Cu_2S. *Geophys Res Lett* 14:135–138.
32. Jahan S, Liton MNH, Khan MKR, Mozibur Rahman M (2015) Effect of aluminum doping on the properties of spray deposited copper sulfide (Cu_2S) thin films. *Int J Adv Eng Technol* 6:23–27.
33. Buerger MJ, Wuensch BJ (1963) The crystal structure of chalcocite, Cu2S. *Mineral Soc Am, Spec Pap* 1:164–170.